# Computational homogenization of microfractured continua using weakly periodic boundary conditions

Erik Svenning*, Martin Fagerström, Fredrik Larsson

*Division of Material and Computational Mechanics*
*Department of Applied Mechanics*
*Chalmers University of Technology*
*Gothenburg, Sweden*

**Abstract**

Computational homogenization of elastic media with stationary cracks is considered, whereby the macroscale stress is obtained by solving a boundary value problem on a Statistical Volume Element (SVE) and the cracks are represented by means of the eXtended Finite Element Method (XFEM). With the presence of cracks on the microscale, conventional BCs (Dirichlet, Neumann, strong periodic) perform poorly, in particular when cracks intersect the SVE boundary. As a remedy, we herein propose to use a mixed variational format to impose periodic boundary conditions in a weak sense on the SVE. Within this framework, we develop a novel traction approximation that is suitable when cracks intersect the SVE boundary. Our main result is the proposition of a stable traction approximation that is piecewise constant between crack-boundary intersections. In particular, we prove analytically that the proposed approximation is stable in terms of the LBB (inf-sup) condition and illustrate the stability properties with a numerical example. We emphasize that the stability analysis is carried out within the setting of weakly periodic boundary conditions, but it also applies to other mixed problems with similar structure, e.g. contact problems. The numerical ex-

*Corresponding author.
*Email address:* erik.svenning@chalmers.se (Erik Svenning)

amples show that the proposed traction approximation is more efficient than conventional boundary conditions (Dirichlet, Neumann, strong periodic) in terms of convergence with increasing SVE size.

*Keywords:* XFEM, Multiscale modeling, Microcracks, LBB (inf-sup), Computational Homogenization, Weak periodicity

## 1. Introduction

Computational homogenization [1, 2] offers the possibility to model the effective response of microheterogeneous materials in numerical simulations. The standard approach is to homogenize the response of a Statistical Volume Element (SVE)[1], whereby the choice of suitable boundary conditions (BCs) on the SVE is critical. It should be noted that conventional BCs (Neumann, Dirichlet and strong periodic [4, 5]) are inaccurate if cracks are present in the microstructure. In particular, Neumann BCs result in severe underestimation of the effective stiffness if cracks cause a piece of the microstructure to be "cut loose" close to the SVE boundary. On the other hand, Dirichlet BCs as well as strong periodic BCs suppress crack opening at the SVE boundary, leading to overstiff predictions. To illustrate these deficiencies, consider the SVE shown in Figure 1, with traction free cracks and linear elastic bulk material. Applying a macroscopic strain of $\bar{\epsilon}_{xx} = 0.1$, $\bar{\epsilon}_{yy} = 0.1$, $\bar{\epsilon}_{xy} = 0$ using Dirichlet, Strong periodic and Neumann boundary conditions gives the qualitative behavior shown in Figure 2. We note that Dirichlet BCs as well as strong periodic BCs enforce crack closure on the SVE boundary, leading to overstiff predictions. Neumann BCs predict very low stresses, leading to severe underprediction of the stiffness.

In the present work, we aim to alleviate the deficiencies illustrated above by proposing boundary conditions that are free of artificial crack closure on the SVE boundary without severely underestimating the effective stiffness. We recognize that the so-called window method, initially proposed by Babuška et al. [6], could be a suitable alternative to be investigated for our purposes. This since the window method has indicated to show faster convergence than Dirichlet and Neumann BCs and since it is readily applicable

[1]We prefer the notation SVE over Representative Volume Element (RVE), since a volume element of finite size will, in general, not be truly representative, cf. Ostoja-Starzewski [3]

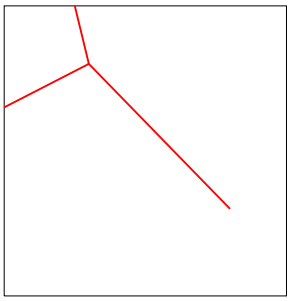

Figure 1: SVE used for illustration of the problems associated to conventional BCs.

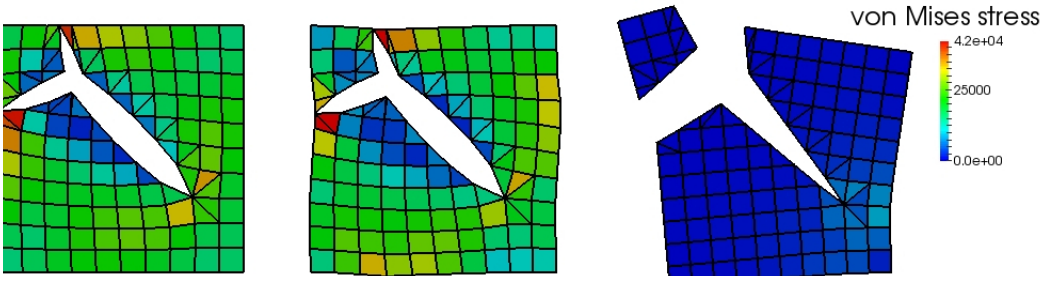


Figure 2: SVE subject to a macroscopic strain of $\bar{\epsilon}_{xx} = 0.1$, $\bar{\epsilon}_{yy} = 0.1$, $\bar{\epsilon}_{xy} = 0$: Qualitative comparison of Dirichlet BCs (left), Strong periodic BCs (center) and Neumann BCs (right).

when voids (or cracks) are present at the boundary, in contrast to strong periodic boundary conditions in their standard form [7]. In this method, the SVE is embedded into a frame of a homogeneous material with a stiffness (updated iteratively) that matches the homogenized response of the SVE. This could potentially overcome some of the overstiffening effects obtained when enforcing crack closure at the boundaries using Dirichlet or strong periodic BCs.

However, in order to avoid the add-ons from the window method (iterative update of the stiffness of the frame material and an enlarged SVE), we instead develop a weak format of microperiodicity in the spirit of [6], restricting ourselves in the first step to microstructures with stationary cracks. Within this framework, we propose a novel piecewise constant traction approximation, that is free from artificial crack closure on the SVE boundary without leading to severe underestimation of the effective stiffness. In particular, we show analytically that the LBB (inf-sup) condition is fulfilled for the proposed discretization and give a numerical example illustrating the stability

properties of the approximation. We also give numerical examples showing that the proposed approximation performs well in terms of convergence with increasing SVE size.

Regarding crack modeling, we note that several options are available, e.g. embedded discontinuities [8], cohesive zone elements (i.e. inter-element cracks) [9] or the Extended Finite Element Method (XFEM) [10, 11, 12]. In the present work, we choose to use XFEM, but any of the approaches mentioned above could be used together with weak periodicity. An advantage of XFEM is that it allows accurate modeling of both discontinuities and strong gradients (or even singularities) in the solution field and its derivatives. In particular, XFEM has been successfully applied to brittle cracks by adding a step enrichment in completely cut elements and enriching with singular asymptotic functions close to crack tips [13]. We note that various features of more complex crack problems can be included in an XFEM framework. For example, branching or intersecting cracks can be modeled by employing special enrichments at the crack intersections [14]. Furthermore, it is possible to model contact and friction along the crack faces in an XFEM setting [15]. Intersecting cracks are considered in the present work, but we will only consider traction free cracks, since we are primarily interested in the performance of different boundary conditions for the SVE problem.

We remark that the present work is concerned with homogenization of microstructures containing *stationary* cracks. Hence, we postpone the difficult question of how to properly treat macroscopic strain localization, see e.g. the percolation path aligned BCs in [16, 17, 18] or the Multiscale Aggregating Discontinuities ($MAD$) method by Belytschko et al. [19]

The remainder of the paper is organized as follows: We start by presenting the variational format of the resolved problem in Section 2 and proceed by employing variationally consistent homogenization to arrive at an expression for the effective macroscale stress in Section 3. The resulting SVE problem is presented in Section 4, followed by a brief description of the crack modeling in Section 5 and a detailed discussion on the construction of the traction mesh in Section 6, where we also discuss stability and solvability of the mixed variational format. More precisely, we propose a piecewise constant traction approximation, with traction discontinuities at crack-boundary intersections and SVE corners, and prove solvability for this discretization. The numerical examples presented in Section 7 show that the prediction of effective stiffness depends strongly on the choice of boundary conditions and traction discretization. In particular, the proposed piecewise constant trac-

tion approximation performs well. Some final remarks and a short summary conclude the paper in Section 8.

## 2. A fractured continuum

In order to establish the weak form of the resolved problem (before introducing homogenization), we consider a domain $\Omega$ with external boundary $\Gamma$. The specimen contains cracks, represented by internal boundaries $\Gamma_{int}$ with predefined normal $\boldsymbol{n}_{int}$ as shown in Figure 3. More precisely, the internal boundary $\Gamma_{int}$ is a two-sided surface, with a positive side $\Gamma_{int}^+$ and a negative side $\Gamma_{int}^-$. $\boldsymbol{n}_{int}$ is taken as the outward unit normal on $\Gamma_{int}^-$, $\boldsymbol{n}_{int} \stackrel{\text{def}}{=} \boldsymbol{n}_{int}^-$. The domain boundary therefore consists of the external boundary and the internal crack boundaries:

$$\partial\Omega = \Gamma_{ext} \cup \Gamma_{int}^+ \cup \Gamma_{int}^-.$$

The external boundary $\Gamma_{ext}$ consists of a part $\Gamma_{ext,D}$ with Dirichlet boundary conditions and a part $\Gamma_{ext,N}$ with Neumann boundary conditions. In the following, we let superscripts $^+$ and $^-$ define quantities on $\Gamma_{int}^+$ and $\Gamma_{int}^-$, respectively. Furthermore, we define the jump of a quantity over the internal boundary as $[\![\boldsymbol{u}]\!] \stackrel{\text{def}}{=} \boldsymbol{u}^+ - \boldsymbol{u}^-$.

Assuming small strains, the quasistatic equilibrium equations are given by

$$\begin{aligned} -\boldsymbol{\sigma} \cdot \boldsymbol{\nabla} &= \boldsymbol{f} \text{ in } \Omega, \\ \boldsymbol{t}^+ + \boldsymbol{t}^- &= \boldsymbol{0} \text{ on } \Gamma_{int}, \\ \boldsymbol{t} &= \hat{\boldsymbol{t}} \text{ on } \Gamma_{ext,N}, \\ \boldsymbol{u} &= \hat{\boldsymbol{u}} \text{ on } \Gamma_{ext,D}, \end{aligned} \tag{1}$$

where $\boldsymbol{\sigma} = \boldsymbol{\sigma}([\boldsymbol{u} \otimes \boldsymbol{\nabla}]^{sym})$ is the Cauchy stress, $\boldsymbol{\nabla}$ is the gradient operator, $\boldsymbol{f}$ is the body force, $\hat{\boldsymbol{t}}$ is a prescribed traction and $\hat{\boldsymbol{u}}$ is a prescribed displacement. Furthermore,

$$\begin{aligned} \boldsymbol{t}^+ &= -\boldsymbol{\sigma}|_{\Gamma_{int}^+} \cdot \boldsymbol{n}_{int}, \\ \boldsymbol{t}^- &= \quad \boldsymbol{\sigma}|_{\Gamma_{int}^-} \cdot \boldsymbol{n}_{int}. \end{aligned}$$

A cohesive zone law may be postulated to describe $\boldsymbol{t} = \boldsymbol{t}^+ = -\boldsymbol{t}^-$ in terms of the jump $[\![\boldsymbol{u}]\!]$ over the internal boundary.

The weak form corresponding to Equation (1) is given by: Find $\boldsymbol{u} \in \mathbb{U}$ such that

$$\int_\Omega \boldsymbol{\sigma} : [\delta\boldsymbol{u} \otimes \boldsymbol{\nabla}] \, \mathrm{d}\Omega - \int_{\Gamma_{int}^+} \boldsymbol{t} \cdot [\![\delta\boldsymbol{u}]\!] \, \mathrm{d}\Gamma = \int_\Omega \boldsymbol{f} \cdot \delta\boldsymbol{u} \, \mathrm{d}\Omega + \int_{\Gamma_{ext}} \hat{\boldsymbol{t}} \cdot \delta\boldsymbol{u} \, \mathrm{d}\Gamma \;\; \forall \delta\boldsymbol{u} \in \mathbb{U}^0,$$
$$\mathbb{U} = \left\{ \boldsymbol{v} \in \left[\mathbb{H}^1(\Omega)\right]^d, \;\; \boldsymbol{v} = \hat{\boldsymbol{u}} \text{ on } \Gamma_{ext,D} \right\},$$
$$\mathbb{U}^0 = \left\{ \boldsymbol{v} \in \left[\mathbb{H}^1(\Omega)\right]^d, \;\; \boldsymbol{v} = \boldsymbol{0} \text{ on } \Gamma_{ext,D} \right\}, \tag{2}$$

where $\mathbb{H}^1(\Omega)$ denotes the (Sobolev) space of functions with square integrable gradients on $\Omega$, and $d$ denotes the dimension of the problem. We note that $\boldsymbol{u}$ and $\delta\boldsymbol{u}$ do not need to be continuous across $\Gamma_{int}$.

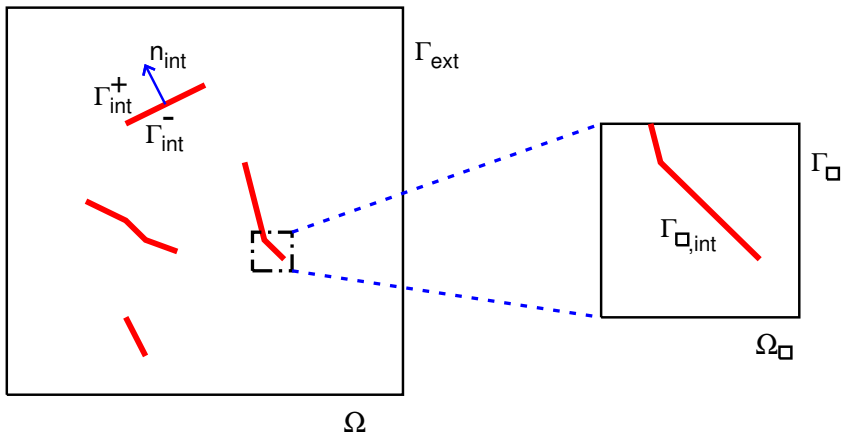


Figure 3: Domain $\Omega$ with external boundary $\Gamma_{ext}$ and internal boundaries $\Gamma_{int}$. An SVE with domain $\Omega_\square$ and boundary $\Gamma_\square$ is also shown.

## 3. Variationally consistent homogenization - macroscale problem

In order to derive an expression for the effective macroscale stress, we consider a macroscopically homogeneous domain $\bar{\Omega} = \Omega \cup \Gamma_{int}$. We wish to replace integrals over the nonsmooth domain $\Omega$ and the internal boundaries

$\Gamma_{int}$ by a "quadrature"[2] for the macroscopically homogeneous domain $\bar{\Omega}$. Hence, a running average is introduced according to

$$\int_{\Omega} y \,\mathrm{d}\Omega - \int_{\Gamma^+_{int}} z \,\mathrm{d}\Gamma \to \int_{\bar{\Omega}} \frac{1}{|\Omega_\square|} \left( \int_{\Omega_\square} y \,\mathrm{d}\Omega - \int_{\Gamma^+_{\square,int}} z \,\mathrm{d}\Gamma \right) \mathrm{d}\Omega, \tag{3}$$

where $\Omega_\square$ is a Statistical Volume Element (SVE), and $\Gamma^+_{\square,int} = \Gamma^+_{int} \cap \Omega_\square$ is the part of the internal boundary located inside $\Omega_\square$.

We introduce the smoothing approximation given by Equation (3) in Equation (2) to get

$$\begin{aligned} &\int_{\bar{\Omega}} \frac{1}{|\Omega_\square|} \left( \int_{\Omega_\square} \boldsymbol{\sigma} : [\delta \boldsymbol{u} \otimes \boldsymbol{\nabla}] \,\mathrm{d}\Omega - \int_{\Gamma^+_{\square,int}} \boldsymbol{t} \cdot [\![ \delta \boldsymbol{u} ]\!] \,\mathrm{d}\Gamma \right) \mathrm{d}\Omega = \\ &= \int_{\bar{\Omega}} \frac{1}{|\Omega_\square|} \left( \int_{\Omega_\square} \boldsymbol{f} \cdot \delta \boldsymbol{u} \,\mathrm{d}\Omega \right) \mathrm{d}\Omega + \int_{\Gamma_{ext}} \hat{\boldsymbol{t}} \cdot \delta \boldsymbol{u} \,\mathrm{d}\Gamma. \end{aligned} \tag{4}$$

In each SVE, the solution field $\boldsymbol{u}$ is split into a smooth part $\boldsymbol{u}^{\mathrm{M}}$ and a subscale fluctuation $\boldsymbol{u}^{\mathrm{s}}$ according to $\boldsymbol{u} = \boldsymbol{u}^{\mathrm{M}} + \boldsymbol{u}^{\mathrm{s}}$. First order homogenization is used, implying that $\boldsymbol{u}^{\mathrm{M}}$ varies linearly within each SVE. Hence, $\boldsymbol{u}^{\mathrm{M}}$ can be expressed in terms of the macroscale displacement $\bar{\boldsymbol{u}}$ for any $\boldsymbol{x}$ in the SVE as

$$\boldsymbol{u}^{\mathrm{M}} = \bar{\boldsymbol{u}} + (\bar{\boldsymbol{u}} \otimes \boldsymbol{\nabla}) \cdot [\boldsymbol{x} - \bar{\boldsymbol{x}}] \tag{5}$$

where $\bar{\boldsymbol{x}} = \frac{1}{|\Omega_\square|} \int_{\Omega_\square} \boldsymbol{x} \,\mathrm{d}\Omega$ and $\bar{\boldsymbol{u}} \otimes \boldsymbol{\nabla}$ is the gradient of the macroscale displacement evaluated at $\bar{\boldsymbol{x}}$. To find the weak form of the macroscale problem, we take the variation of Equation (5) to obtain

$$\delta \boldsymbol{u}^{\mathrm{M}} = \delta \bar{\boldsymbol{u}} + (\delta \bar{\boldsymbol{u}} \otimes \boldsymbol{\nabla}) \cdot [\boldsymbol{x} - \bar{\boldsymbol{x}}]$$

on each $\Omega_\square$. Hence, the task is to find $\bar{\boldsymbol{u}} \in \bar{\mathbb{U}}$ that solves

$$\begin{aligned} \int_{\bar{\Omega}} \bar{\boldsymbol{\sigma}} : [\delta \bar{\boldsymbol{u}} \otimes \boldsymbol{\nabla}] \,\mathrm{d}\Omega = \int_{\bar{\Omega}} \bar{\boldsymbol{f}} \cdot \delta \bar{\boldsymbol{u}} + \bar{\boldsymbol{f}}^{(2)} : [\delta \bar{\boldsymbol{u}} \otimes \boldsymbol{\nabla}] \,\mathrm{d}\Omega + \int_{\Gamma_{ext,N}} \hat{\boldsymbol{t}} \cdot \delta \bar{\boldsymbol{u}} \,\mathrm{d}\Gamma \;\; \forall \delta \bar{\boldsymbol{u}} \in \bar{\mathbb{U}}^0, \\ \bar{\mathbb{U}} = \left\{ \boldsymbol{v} \in \left[ \mathbb{H}^1(\bar{\Omega}) \right]^d, \;\; \boldsymbol{v} = \hat{\boldsymbol{u}} \text{ on } \Gamma_{ext,D} \right\}, \\ \bar{\mathbb{U}}^0 = \left\{ \boldsymbol{v} \in \left[ \mathbb{H}^1(\bar{\Omega}) \right]^d, \;\; \boldsymbol{v} = \boldsymbol{0} \text{ on } \Gamma_{ext,D} \right\}, \end{aligned} \tag{6}$$

[2]Note that an identical formulation results from choosing $\Omega = \cup \Omega_\square$ and interpreting the integrand on $\bar{\Omega}$ to be piecewise constant in each $\bar{\Omega}_\square$.

where

$$\bar{\boldsymbol{f}} \stackrel{\text{def}}{=} \frac{1}{|\Omega_\square|} \int_{\Omega_\square} \boldsymbol{f} \, \mathrm{d}\Omega,$$
$$\bar{\boldsymbol{f}}^{(2)} \stackrel{\text{def}}{=} \frac{1}{|\Omega_\square|} \int_{\Omega_\square} \boldsymbol{f} \otimes [\boldsymbol{x} - \bar{\boldsymbol{x}}] \, \mathrm{d}\Omega,$$

and the effective macroscale stress is

$$\bar{\boldsymbol{\sigma}} \stackrel{\text{def}}{=} \frac{1}{|\Omega_\square|} \int_{\Omega_\square} \boldsymbol{\sigma} \, \mathrm{d}\Omega. \tag{7}$$

**Remark.** The last identity in Equation (7) follows from the assumption of continuous $\boldsymbol{u}^{\mathrm{M}}$. Hence, macroscopic localization is not considered in the present work.

**Remark.** Only volume homogenization is considered in the present work. Hence, we assume $\boldsymbol{u} \equiv \bar{\boldsymbol{u}}$ on the external boundary $\Gamma_{ext}$.

## 4. Microscale problem

Prolongation conditions defining the relation between $\boldsymbol{u}$ and $\bar{\boldsymbol{u}}$ need to be specified to obtain the effective relation $\bar{\boldsymbol{\sigma}}\{\bar{\boldsymbol{u}}, \bar{\boldsymbol{u}} \otimes \boldsymbol{\nabla}\}$, cf. Equation (6). In light of Equation (5), we choose the coupling

$$\bar{\boldsymbol{u}} \stackrel{\text{def}}{=} \frac{1}{|\Gamma_\square|} \int_{\Gamma_\square} \boldsymbol{u} \, \mathrm{d}\Gamma, \qquad \bar{\boldsymbol{u}} \otimes \boldsymbol{\nabla} \stackrel{\text{def}}{=} \frac{1}{|\Omega_\square|} \int_{\Gamma_\square} \boldsymbol{u} \otimes \boldsymbol{n} \, \mathrm{d}\Gamma. \tag{8}$$

We note that $\bar{\boldsymbol{u}} \otimes \boldsymbol{\nabla}$ is equal to the volume average of $\boldsymbol{u} \otimes \boldsymbol{\nabla}$ if no internal boundaries (e.g. cracks) are present in the SVE. However, equality does not hold when open cracks are present in the SVE. Thereby, we choose the definition given by Equation (8) because it measures the effective deformation and translation of the SVE frame independent of presence of cracks inside the SVE. Macroscale rigid body translation is here defined in a non-standard fashion along the lines of that for transient problems in [20]. However, since the effective stress response is invariant to any translation, this condition may be expressed in any (reasonable) way we choose, i.e. either by a volume average or by prescribing the displacement of a single node for a finite element discretization.

Next, we turn to the definition of quantities on the SVE boundary. First, we divide the SVE boundary into an image part $\Gamma_\square^+$ and a mirror part $\Gamma_\square^-$ as

shown in Figure 4. Furthermore, we introduce a mapping $\boldsymbol{\varphi}_{per} : \Gamma_{\square}^{+} \to \Gamma_{\square}^{-}$ such that points on $\Gamma_{\square}^{+}$ and $\Gamma_{\square}^{-}$ are associated to each other according to $\boldsymbol{x}^{-} = \boldsymbol{\varphi}_{per}(\boldsymbol{x}^{+})$. We define the jump between a point $\boldsymbol{x}^{+}$ on $\Gamma_{\square}^{+}$ and the associated point $\boldsymbol{x}^{-} = \boldsymbol{\varphi}_{per}(\boldsymbol{x}^{+})$ on $\Gamma_{\square}^{-}$ as

$$[\![\boldsymbol{u}]\!]_{\square} \overset{\text{def}}{=} \boldsymbol{u}_{\Gamma_{\square}^{+}} - \boldsymbol{u}_{\Gamma_{\square}^{-}} = \boldsymbol{u} - \boldsymbol{u} \circ \boldsymbol{\varphi}_{per} \text{ on } \Gamma_{\square}^{+}.$$

Strong periodicity is obtained by prescribing periodic displacements and antiperiodic tractions. More precisely, in the case of strong periodicity, we require

$$[\![\boldsymbol{u}]\!]_{\square} = \bar{\boldsymbol{\epsilon}} \cdot [\![\boldsymbol{x} - \bar{\boldsymbol{x}}]\!]_{\square} \qquad \text{on } \Gamma_{\square}^{+}, \tag{9}$$

$$\boldsymbol{t}^{+} + \boldsymbol{t}^{-} = \boldsymbol{0} \qquad \text{on } \Gamma_{\square}^{+}, \tag{10}$$

$$\frac{1}{|\Gamma_{\square}|} \int_{\Gamma_{\square}} \boldsymbol{u} \, \mathrm{d}\Gamma = \boldsymbol{0}, \tag{11}$$

where $\bar{\boldsymbol{\epsilon}} \overset{\text{def}}{=} [\bar{\boldsymbol{u}} \otimes \boldsymbol{\nabla}]^{sym}$. Strong periodicity requires Equation (9) and Equation (10) to hold pointwise on $\Gamma_{\square}^{+}$. In the present work, we instead assume that the subscale field is periodic across the SVE boundaries in a weak sense as proposed by Larsson et al.[21]. Thus, we introduce an independent discretization for the boundary traction and require $[\![\boldsymbol{u}]\!]_{\square} = \bar{\boldsymbol{\epsilon}} \cdot [\![\boldsymbol{x} - \bar{\boldsymbol{x}}]\!]_{\square}$ to hold weakly instead of pointwise to get the following SVE problem: Find $\boldsymbol{u} \in \mathbb{U}_{\square}$ and $\boldsymbol{t}_{\lambda} \in \mathbb{T}_{\square}$ such that

$$\begin{aligned} a_{\square}(\boldsymbol{u}, \delta\boldsymbol{u}) - d_{\square}(\boldsymbol{t}_{\lambda}, \delta\boldsymbol{u}) &= 0 \;\; \forall \delta\boldsymbol{u} \in \mathbb{U}_{\square}, \\ -d_{\square}(\delta\boldsymbol{t}_{\lambda}, \boldsymbol{u}) &= -d_{\square}(\delta\boldsymbol{t}_{\lambda}, \bar{\boldsymbol{\epsilon}} \cdot [\boldsymbol{x} - \bar{\boldsymbol{x}}]) \;\; \forall \delta\boldsymbol{t}_{\lambda} \in \mathbb{T}_{\square}, \end{aligned} \tag{12}$$

$$\mathbb{U}_{\square} = \{\boldsymbol{v} \in \left[\mathbb{H}^{1}(\Omega_{\square})\right]^{d}, \; \int_{\Gamma_{\square}} \boldsymbol{v} \, \mathrm{d}\Gamma = \boldsymbol{0}\}, \tag{13}$$

$$\mathbb{T}_{\square} = \{\boldsymbol{t} \in \left[\mathbb{L}_{2}\left(\Gamma_{\square}^{+}\right)\right]^{(d-1)}\}, \tag{14}$$

where we introduced the expressions

$$a_{\square}(\boldsymbol{u}, \delta\boldsymbol{u}) \overset{\text{def}}{=} \frac{1}{|\Omega_{\square}|} \left[ \int_{\Omega_{\square}} \boldsymbol{\sigma} : \boldsymbol{\epsilon}[\delta\boldsymbol{u}] \, \mathrm{d}\Omega - \int_{\Gamma_{\square,int}^{+}} \boldsymbol{t} \cdot [\![\delta\boldsymbol{u}]\!] \, \mathrm{d}\Gamma \right], \tag{15}$$

$$d_{\square}(\boldsymbol{t}_{\lambda}, \delta\boldsymbol{u}) \overset{\text{def}}{=} \frac{1}{|\Omega_{\square}|} \int_{\Gamma_{\square}^{+}} \boldsymbol{t}_{\lambda} \cdot [\![\delta\boldsymbol{u}]\!]_{\square} \, \mathrm{d}\Gamma \tag{16}$$

and where $\mathbb{L}_2\big(\Gamma^+_\square\big)$ denotes the space of square integrable functions on $\Gamma^+_\square$.

Solving Equation (12) and employing Equation (7) allows $\bar{\boldsymbol{\sigma}} = \bar{\boldsymbol{\sigma}}\{\bar{\boldsymbol{\epsilon}}\}$ to be computed. As to the complete prolongation conditions in Equation (8), we remark that Equation (11) and Equation (9) correspond to $\bar{\boldsymbol{u}} = \boldsymbol{0}$ and $\bar{\boldsymbol{u}} \otimes \boldsymbol{\nabla} = \bar{\boldsymbol{\epsilon}}$. We note, however, that the effective stress response $\bar{\boldsymbol{\sigma}}$ would be invariant to any $\bar{\boldsymbol{u}} \neq \boldsymbol{0}$ and $[\bar{\boldsymbol{u}} \otimes \boldsymbol{\nabla}]^{skw} \neq \boldsymbol{0}$.

In a continuous setting, the second identity in Equation (12) is fulfilled for all $\delta \boldsymbol{t}_\lambda \in \mathbb{T}_\square$, so that $\boldsymbol{u} = \bar{\boldsymbol{\epsilon}} \cdot [\![\boldsymbol{x} - \bar{\boldsymbol{x}}]\!]_\square$ holds pointwise on $\Gamma^+_\square$. Hence, strong microperiodicity is fulfilled in the continuous setting. On the other hand, coarsening of $\mathbb{U}_\square$ and $\mathbb{T}_\square$ leads to different modeling, due to weak fulfillment of the second identity in Equation (12). Dirichlet and Neumann boundary conditions are obtained by restricting the spaces $\mathbb{U}_\square$ and $\mathbb{T}_\square$, respectively. More precisely, Neumann boundary conditions are obtained as the coarsest possible traction discretization, with piecewise constant traction on each face of the SVE.

Furthermore, we note that $\boldsymbol{u}$ as well as $\boldsymbol{t}_\lambda$ are discontinuous on $\Gamma_\square$ where cracks intersect the SVE boundary as discussed further below. Before proceeding, we also remark that the Hill-Mandel condition is satisfied for arbitrary choices of $\mathbb{U}^h_\square$ and $\mathbb{T}^h_\square$ [21].

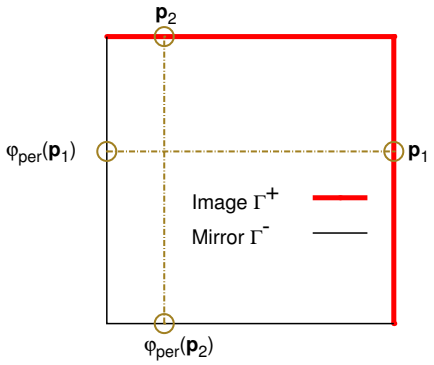


Figure 4: Statistical Volume Element (SVE) with boundary divided into image and mirror parts.

## 5. Crack modeling

Solving the mixed variational form, Equation (12), when cracks are present in the SVE requires that displacement discontinuities across cracks are properly taken into account in $\mathbb{U}^h_\square$. In the present work, we choose to use an XFEM approximation to account for displacement discontinuities, see e.g. the classical work by Belytschko and Black [10] or the review by Fries and Belytschko [12]. Regarding the numerical treatment of intersecting cracks, as also considered herein, see Daux et al. [14].

We note that numerical problems occur if a part of the microstructure is completely cut loose by cracks, because the thereby emerging but irrelevant[3] rigid body motion will not be prevented in the piece cut loose. In order to obtain a solvable problem even if this occurs, we use an elastic cohesive zone, with very low stiffness, as regularization. We remark that this regularization is added to avoid unrestricted rigid body *displacement* in the SVE. Hence, this regularization is not related to the stability of the *traction* approximation presented below.

## 6. Stable traction approximations in 2D

### *6.1. Preliminaries*

To solve the mixed variational form in Equation (12), we need to construct a suitable test space $\mathbb{T}^h_\square$ for the boundary traction, e.g. with a global polynomial basis [22] or with a piecewise polynomial approximation represented by a traction mesh on the SVE boundary [21]. In the following, we restrict the analysis to 2D[4], and choose the latter option, i.e. we specify $\mathbb{T}^h_\square$ by dividing $\Gamma^+_\square$ into (one-dimensional) segments $\mathcal{T}_e$ and requiring $\boldsymbol{t}_\lambda$ to be piecewise polynomial on each $\mathcal{T}_e$. Furthermore, we let $\mathcal{Q}$ denote the set of points either where cracks intersect the SVE boundary or where the normal of the SVE boundary is discontinuous (i.e. at SVE corners).

[3] The rigid body motion of a cut loose part will not affect the effective stress result, and thus represents an additional invariant for the system.

[4] We restrict ourselves to 2D in order to simplify the traction mesh generation. We note, however, that both weakly periodic boundary conditions and XFEM are applicable to 3D problems. See e.g. Öhman et al. [23] regarding weakly periodic BCs and Areias et al. [24] regarding XFEM.

We now consider piecewise linear continuous approximations given by

$$\mathbb{T}_{\square}^{h,lin} = \{\boldsymbol{t} \text{ is piecewise linear on each } \mathcal{T}_e \text{ and continuous everywhere except at } \boldsymbol{q}_i \in \mathbb{Q}\}\,. \tag{17}$$

We also consider piecewise constant discontinuous approximations given by

$$\mathbb{T}_{\square}^{h,const} = \{\boldsymbol{t} \text{ is piecewise constant on each } \mathcal{T}_e \text{ with discontinuities at } \boldsymbol{q}_i \in \mathbb{Q}\} \tag{18}$$

as discussed further below.

We note that no special regularity requirements need to be fulfilled by the traction discretization, other than that specified in Equation (14). However, the stability of the mixed formulation in terms of the LBB condition needs to be addressed.

### *6.2. Piecewise linear traction approximation*

To construct a traction mesh suitable for a piecewise linear approximation $\boldsymbol{t}_\lambda \in \mathbb{T}_{\square}^{h,lin}$, we may start by following along the same lines as Larsson et al.[21]. As a first step, all nodes on the image boundary as well as the mirror boundary are projected onto the image boundary as shown in Figure 5. Also, points where cracks intersect the boundary are projected in the same way. The next step is to remove nodes that are closer to each other than a given tolerance, in order to avoid traction elements that are too small, see [21] for details. The mesh obtained in this way, or meshes obtained by coarsening this mesh, as shown to the right in Figure 5, have been shown to give LBB-stable approximations for piecewise linear functions in $\mathbb{U}_{\square}^{h}$ and $\mathbb{T}_{\square}^{h}$ [21].

### *6.3. Lowest order stable approximation*

In the following, we aim to establish the lowest order stable approximation with nontrivial response. As discussed previously, strong periodic BCs (corresponding to well resolved weak periodic BCs) may give overstiff response when cracks are present in the SVE, because strong periodic BCs will close cracks that are not aligned with the periodicity directions. On the other hand, as also discussed above, Neumann BCs (corresponding to weak periodic BCs with the coarsest possible traction discretization) will predict zero stiffness if only a tiny part of the SVE is "cut loose" by cracks. Hence, to find a more suitable BC, we are interested in traction discretizations that are sufficiently fine to predict a stiffness greater than zero, but not so fine

that cracks intersecting the boundary are forced to be closed. To this end, we propose a piecewise constant traction approximation $\boldsymbol{t}_\lambda \in \mathbb{T}_\square^{h,const}$, with traction discontinuities only at the SVE corners and where cracks intersect the boundary only, as shown in Figure 6. This discretization is stable in terms of the LBB condition as we prove below.

*6.4. Proof of stability*

It is known that a piecewise constant traction approximation on each linear displacement element fails to fulfill the LBB condition, cf. El-Abbasi and Bathe [25] in the context of contact. Therefore, the stability of the piecewise constant traction approximation $\boldsymbol{t}_\lambda \in \mathbb{T}_\square^{h,const}$ proposed above needs to be studied in detail. In order to ensure existence and uniqueness of the solution for the special case considered in our work, we need to ensure that

$$\inf_{\mathbf{0}\neq\boldsymbol{t}_\lambda\in\mathbb{T}_\square} \sup_{\mathbf{0}\neq\boldsymbol{u}\in\mathbb{U}_\square} \frac{d_\square(\boldsymbol{t}_\lambda,\boldsymbol{u})}{\|\boldsymbol{t}_\lambda\|_{\mathbb{T}}\|\boldsymbol{u}\|_{\mathbb{U}}} \geq \beta, \tag{19}$$

where $\beta$ is a positive constant and the norms are given by

$$\|\boldsymbol{t}_\lambda\|_{\mathbb{T}} = \sqrt{\int_{\Gamma_\square^+} \boldsymbol{t}_\lambda \cdot \boldsymbol{t}_\lambda \,\mathrm{d}\Gamma}, \tag{20}$$

$$\|\boldsymbol{u}\|_{\mathbb{U}} = \sqrt{a_\square(\boldsymbol{u},\boldsymbol{u})}. \tag{21}$$

We remark that solvability of the discrete problem is guaranteed if Equation (19) is satisfied for the chosen discretization. Furthermore, if $\beta$ is independent of the element size, Equation (19) represents the classic LBB condition, implying numerical stability. To see that Equation (19) is indeed satisfied for the piecewise constant traction approximation shown in Figure 6, we first note that

$$\inf_{\mathbf{0}\neq\boldsymbol{t}_\lambda\in\mathbb{T}_\square} \sup_{\mathbf{0}\neq\boldsymbol{u}\in\mathbb{U}_\square} \frac{d_\square(\boldsymbol{t}_\lambda,\boldsymbol{u})}{\|\boldsymbol{t}_\lambda\|_{\mathbb{T}}\|\boldsymbol{u}\|_{\mathbb{U}}} \geq \inf_{\mathbf{0}\neq\boldsymbol{t}_\lambda\in\mathbb{T}_\square} \frac{d_\square(\boldsymbol{t}_\lambda,\tilde{\boldsymbol{u}})}{\|\boldsymbol{t}_\lambda\|_{\mathbb{T}}\|\tilde{\boldsymbol{u}}\|_{\mathbb{U}}} \tag{22}$$

for an arbitrarily chosen nonzero $\tilde{\boldsymbol{u}} \in \mathbb{U}_\square$. Hence, the proof of stability can be obtained by constructing a $\tilde{\boldsymbol{u}}$ that fulfills Equation (19). To this end, let $\tilde{\boldsymbol{u}}$ be bilinear on each traction element as shown in Figure 7. $\tilde{\boldsymbol{u}}$ is zero at the ends of the traction element and reaches a maximum value $\tilde{\boldsymbol{u}}_i$ somewhere in the element, where $i$ denotes the index of the traction element.

To derive a bound, we now choose the specific amplitude $\tilde{\boldsymbol{u}}_i = 2\boldsymbol{t}_{\lambda i}$. We remark that the maximum point, where $\tilde{\boldsymbol{u}} = \tilde{\boldsymbol{u}}_i$, can be located anywhere within the traction element. In practice, this case corresponds to having at least one (displacement) node somewhere in each traction element. This is a reasonable requirement on a good mesh, and it will always be fulfilled in the limit of a very fine mesh. Furthermore, we set $\tilde{\boldsymbol{u}} = \boldsymbol{0}$ on $\Gamma_\square^-$ as well as along the dashed blue lines shown in Figure 7. For this choice of $\tilde{\boldsymbol{u}}$, it can be shown that $d_\square(\boldsymbol{t}_\lambda, \tilde{\boldsymbol{u}})$ is given by (see Appendix Appendix A)

$$d_\square(\boldsymbol{t}_\lambda, \tilde{\boldsymbol{u}}) = \sum_i (\boldsymbol{t}_{\lambda i} \cdot \boldsymbol{t}_{\lambda i})\, s_i = \int_{\Gamma_\square^+} \boldsymbol{t}_\lambda \cdot \boldsymbol{t}_\lambda \, \mathrm{d}\Gamma = \|\boldsymbol{t}_\lambda\|_{\mathbb{T}}^2. \tag{23}$$

In Appendix Appendix A, we also show that

$$\|\boldsymbol{u}\|_{\mathbb{U}} \leq C_1 \|\boldsymbol{t}_\lambda\|_{\mathbb{T}}, \tag{24}$$

where

$$C_1 = \sqrt{\frac{8\lambda_{max} L_\square}{s_{min}^2}}. \tag{25}$$

In Equation (25) above, $\lambda_{max}$ is the largest eigenvalue of the constitutive stiffness tensor, $L_\square$ is the SVE size and $s_{min}$ is the smallest distance between a traction discontinuity and a point where $\tilde{\boldsymbol{u}} = \tilde{\boldsymbol{u}}_i$ as indicated in Figure 7.

Now, by inserting Equation (23) and Equation (24) in Equation (22), we obtain

$$\inf_{\boldsymbol{0} \neq \boldsymbol{t}_\lambda \in \mathbb{T}_\square} \frac{d_\square(\boldsymbol{t}_\lambda, \tilde{\boldsymbol{u}})}{\|\boldsymbol{t}_\lambda\|_{\mathbb{T}} \|\tilde{\boldsymbol{u}}\|_{\mathbb{U}}} = \inf_{\boldsymbol{0} \neq \boldsymbol{t}_\lambda \in \mathbb{T}_\square} \frac{\|\boldsymbol{t}_\lambda\|_{\mathbb{T}}}{\|\tilde{\boldsymbol{u}}\|_{\mathbb{U}}} \geq \inf_{\boldsymbol{0} \neq \boldsymbol{t}_\lambda \in \mathbb{T}_\square} \frac{\|\boldsymbol{t}_\lambda\|_{\mathbb{T}}}{C_1 \|\boldsymbol{t}_\lambda\|_{\mathbb{T}}} = \frac{1}{C_1}. \tag{26}$$

Comparing with Equation (19), we have

$$\inf_{\boldsymbol{0} \neq \boldsymbol{t}_\lambda \in \mathbb{T}_\square} \sup_{\boldsymbol{0} \neq \boldsymbol{u} \in \mathbb{U}_\square} \frac{d_\square(\boldsymbol{t}_\lambda, \boldsymbol{u})}{\|\boldsymbol{t}_\lambda\|_{\mathbb{T}} \|\boldsymbol{u}\|_{\mathbb{U}}} \geq \frac{1}{C_1} > 0, \tag{27}$$

where the constant $C_1 = \sqrt{\frac{8\lambda_{max} L_\square}{s_{min}^2}}$ is positive and independent of the mesh size. Hence, Equation (19) is fulfilled for the discrete problem, provided that there is at least one (displacement) node within each traction element.

*6.5. Implications of stability analysis*

We have shown that a traction approximation that is piecewise constant between crack-boundary intersections is stable provided that the displacement approximation allows a bilinear displacement on each traction element as shown in Figure 7. This condition is fulfilled if the displacement mesh has at least one node inside each traction element. A simple example of stable and unstable approximations is given in Figure 8.

Since fulfillment of the LBB condition requires $C_1$ to be independent of the mesh size, the size of the traction elements must be kept fixed when refining the displacement mesh. This is the case here, where the traction mesh is constructed from the location of crack-boundary intersections that do not change under mesh refinement. Refining the traction mesh together with the displacement mesh would cause $s_{min}$ to decrease under mesh refinement and hence $\frac{1}{C_1}$ would tend to zero, which would imply violation of the LBB condition as given by Equation (19).

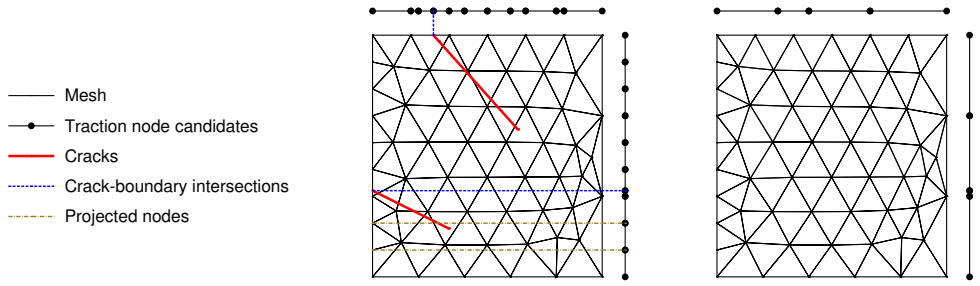


Figure 5: Traction discretization: unprocessed (left) and processed (right) traction meshes. Addition of traction nodes where cracks intersect the boundary is indicated to the left.

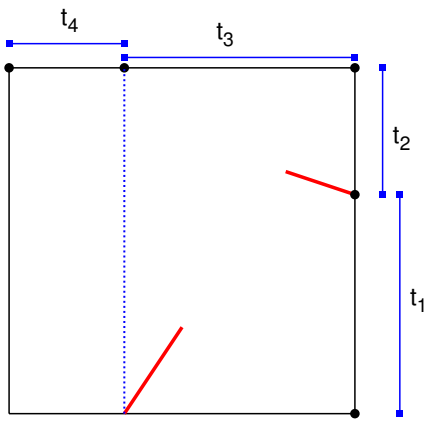


Figure 6: Piecewise constant traction approximation with traction discontinuities at SVE boundaries and crack-boundary intersections.

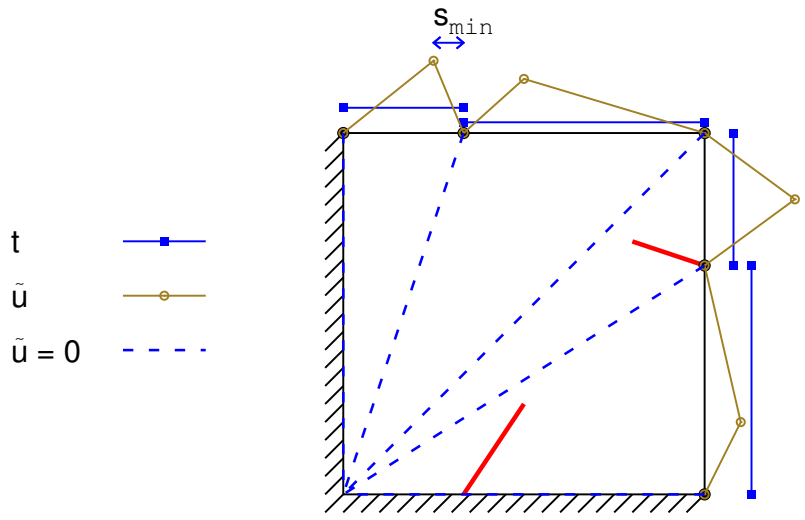


Figure 7: Definition of $\tilde{\boldsymbol{u}}$ for solvability considerations: $\tilde{\boldsymbol{u}}$ is bilinear on each traction element.

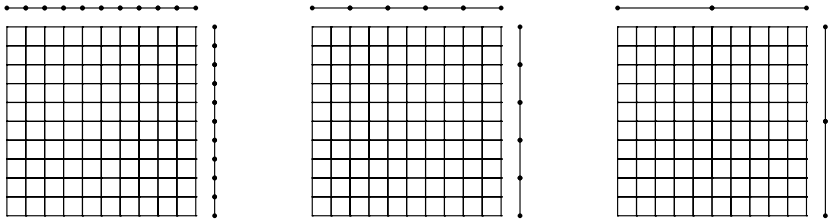

(a) Mesh A. (b) Mesh B. (c) Mesh C.

Figure 8: Traction meshes for illustration of the stability analysis: Mesh A gives unstable response whereas Mesh B and Mesh C give stable response (provided that the traction mesh is kept fixed when refining the displacement mesh).

## 7. Numerical examples

In this section, we first demonstrate the implications of the stability analysis by solving a simple problem using stable and unstable traction approximations in Section 7.1.

Since first order homogenization is used, a Representative Volume Element (RVE) that gives the "exact" unique response needs to be infinitely large. Hence, subsequent to the stability analysis, in this section we also study how large the SVE needs to be in order to obtain accurate results. We start with an example of a periodic microstructure in Section 7.2, in order to show the convergence properties of the formulation in a simple case. To show the behavior of different BCs when cracks intersect the SVE boundary, we then proceed by analyzing a single realization of a random microstructure in Section 7.3. Finally, we consider several realizations of a random microstructure in Section 7.4, in order to obtain results of average properties.

In all examples, we consider a two-dimensional linear elastic microstructure. Plane strain and quasistatic loading is assumed. Following standard procedures, the cracks are modeled with a combination of Heaviside enrichment in completely cut elements and asymptotic enrichments in tip elements.

For the examples in Sections 7.2, 7.3 and 7.4, we consider a material with Young's modulus $E = 210\,\text{MPa}$ and Poisson's ratio $\nu = 0.3$. The element size is kept fixed and a (displacement) mesh consisting of $10 \times 10$ 4-node quadrilaterals is used for the smallest SVE in all analyses[5].

To analyze the results of the numerical simulations, we will study the smallest eigenvalue of the effective stiffness tensor. The reason for showing the smallest eigenvalue, rather than e.g. the largest, is that the smallest eigenvalue better captures the sensitivity (or insensitivity) to spurious softening for different boundary conditions.

The model has been implemented in the open source code OOFEM [26, 27].

### *7.1. Stability of the mixed formulation*

As a supplement to the analytical stability proof provided in Section 6.4, we will illustrate the assumptions behind the proof with a numerical example. The proof states that the LBB condition is fulfilled if at least one

[5]This is sufficient because asymptotic enrichment functions are used in elements containing crack tips.

displacement node is located inside each traction element and the size of the traction elements is kept constant when refining the displacement elements.

To illustrate this condition with the simplest possible example, we consider a homogeneous SVE (pure, homogeneous material without cracks or inclusions) discretized with $10 \times 10$ quadrilateral elements. The material is linear elastic with Young's modulus $E = 10$ and Poisson's ratio $\nu = 0.3$. We use weakly periodic boundary conditions to apply a uniaxial effective strain $\bar{\epsilon}_{xx} = 1$.

Three different traction meshes are considered as shown in Figure 8. We note that Mesh B and Mesh C have at least one displacement node inside each traction element, so we expect these discretizations to give stable response. However, Mesh A does not meet this requirement, so we cannot expect Mesh A to give stable response. Solving the SVE problem with these three meshes and computing the condition number of the global stiffness matrix gives the following result:

- Mesh A gives a condition number of $10^{25}$,
- Mesh B gives a condition number of $10^{8}$,
- Mesh C gives a condition number of $10^{7}$.

Mesh A results in a very high condition number that indicates numerical problems, whereas Mesh B and Mesh C lead to well conditioned matrices. Furthermore, the instability indicated by the high condition number obtained with Mesh A pollutes the solution for the boundary traction as shown in Figure 9: Mesh B and Mesh C lead to smooth boundary tractions, whereas Mesh A leads to an oscillatory solution.

With the simple example above in mind, we emphasize that the piecewise constant traction approximation is stable provided that:

1. At least one displacement node is located inside each traction element. This is a reasonable assumption for a sufficiently fine displacement mesh, provided that the traction elements are not allowed to be too small (see also the discussion on removing traction nodes that are too close in [21]).
2. The length of the traction elements must not tend to zero as the displacement elements are refined. This requirement is fulfilled in the present work, because the traction mesh is created based on the locations of cracks or grain boundaries, and these positions do not change under mesh refinement.

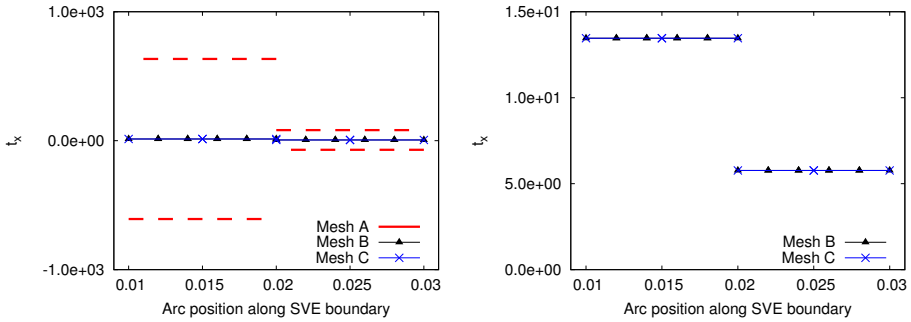


(a) Y-axis range from $-1.0 \cdot 10^3$ to $1.0 \cdot 10^3$.

(b) Y-axis range from 0.0 to 15.0.

Figure 9: Traction along $\Gamma^+_\square$ computed with different traction meshes. We display the results with a wide y-axis range (left) to show the oscillatory response obtained with Mesh A and a zoomed in plot (right) to show the smooth response obtained with Mesh B and Mesh C. We note that the densest traction discretization (Mesh A) is unstable. (We also note that the traction is discontinuous across the SVE corner, since the normal of the boundary is discontinuous there.)

### *7.2. Cracks in a periodic microstructure*

In this example, we consider cracks in a periodic microstructure and investigate the effect of different piecewise linear traction discretizations. The microstructure considered, with a unit cell length of 10 µm, is shown in Figure 10. A crack of length $L_c = 5$ µm is centered in the unit cell and oriented such that the angle to the horizontal axis is 30 degrees.

The smallest eigenvalue of the effective stiffness tensor, computed with Dirichlet, Neumann and strong periodic boundary conditions, is shown in Figure 11. We note, as expected, that Dirichlet boundary conditions converge from above while Neumann boundary conditions converge from below when increasing the SVE size. Strong periodic boundary conditions are exact for the smallest SVE, because the microstructure is periodic. Keeping these standard results in mind, we proceed and study the performance of weakly periodic BCs with different traction discretizations. In particular, we consider the following coarsenings from the densest piecewise linear traction mesh:

- Mesh **Lin1**: All traction nodes are retained and piecewise linear interpolation is used.

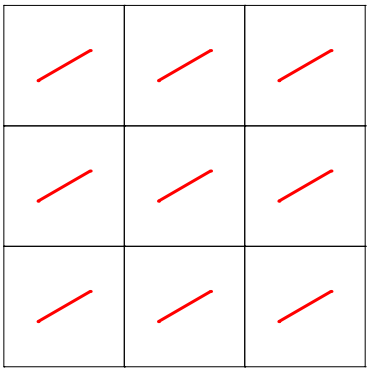

Figure 10: Periodic microstructure with cracks considered in Example 7.2.

- Mesh **Lin2**: Every second traction node is retained and piecewise linear interpolation is used.
- Mesh **Lin3**: Every fifth traction node is retained and piecewise linear interpolation is used.
- Mesh **Lin4**: Coarsest possible traction discretization, only corner nodes are retained and piecewise linear interpolation is used.

Examples of two traction discretizations are shown in Figure 12. The effective stiffness predicted with different traction meshes and piecewise linear traction interpolation is shown in Figure 13. The coarsest possible discretization corresponds to Neumann boundary conditions, while the finest discretization gives strong periodic boundary conditions. It is interesting to note that a traction node spacing of 5, which is the smallest possible refinement from the Neumann case, gives results that are very close to the strong periodic case. For this example, the results thus converge quickly towards the strong periodic solution when refining the traction mesh.

*7.3. Single realization of a random microstructure*

We consider a single realization of a microstructure with randomly distributed cracks. In this example, all cracks are straight and have the same length $L_c = 10\,\mu\text{m}$. A large sample is created and SVEs of different sizes are cut out from the large sample. Figure 14 shows SVEs of a few different sizes.

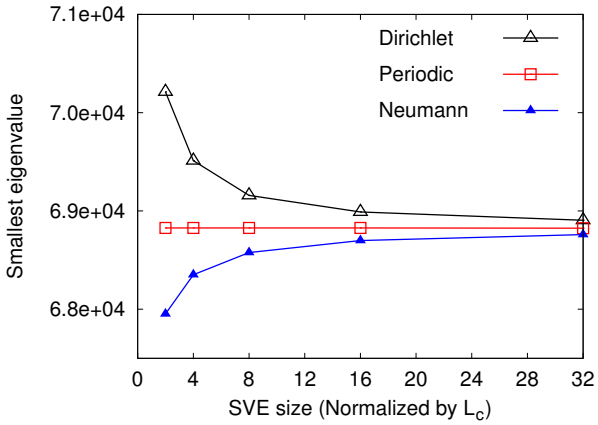


Figure 11: Convergence of effective stiffness for the periodic microstructure considered in Example 7.2.

The effective stiffness of the SVE is computed with Dirichlet, Neumann and weakly periodic boundary conditions. For the weakly periodic BCs, three different traction discretizations are considered:

- Mesh **Lin5**: All traction nodes are retained and piecewise linear interpolation is used.
- Mesh **Lin6**: Only traction nodes located at corners and where cracks intersect the boundary are retained. Piecewise linear interpolation is used.
- Mesh **Const1**: As Lin6, but with piecewise constant interpolation on each traction element. This is the *lowest order stable approximation with nontrivial response* discussed in Section 6.3.

The three discretizations defined above are shown in Figure 15 for the smallest SVE.

The effective stiffness predicted with different BCs and traction discretizations is shown in Figure 16. The stiffness predicted with Dirichlet BCs converges from above, while zero or almost zero stiffness is predicted with Neumann BCs. In general, zero stiffness will be predicted with Neumann BCs if a part of the boundary is completely cut loose by cracks. This phenomenon is increasingly likely to occur somewhere along the boundary when the SVE size increases, and the zero stiffness predicted with Neumann BCs is therefore expected.

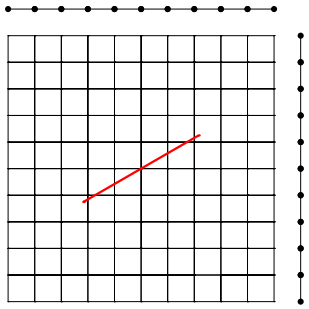

(a) Mesh Lin1: Traction mesh with all nodes retained.

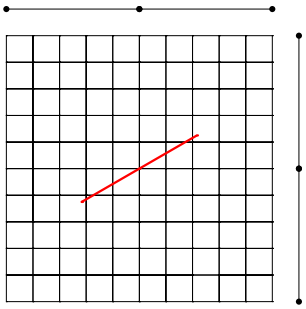

(b) Mesh Lin3: Traction mesh with every fifth node retained.

Figure 12: Different traction discretizations used in Example 7.2.

Turning our attention to the weakly periodic BCs, we note that the solution obtained with Lin5, corresponding to (almost) strong periodic BCs, converges from above and it converges faster than Dirichlet BCs. However, the solution is still notably overstiff. A weaker response is predicted when mesh Lin6 or mesh Const1 is used. We note that the curves in Figure 16 are nonsmooth because the small SVEs are not statistically representative. Hence, our next step is to perform simulations on several realizations of the microstructure and study the convergence of the mean value.

*7.4. Statistical properties of a random microstructure*

In the last example, we consider several realizations of the random microstructure studied in Example 7.3. The number of realizations for each SVE size is chosen such that the 95% confidence interval[6] for the smallest eigenvalue of the effective stiffness is within ±5% of the mean value.

The mean value of the effective stiffness may be computed using Voigt sampling,

$$\mathbf{E}^V = \langle \mathbf{E} \rangle \,, \tag{28}$$

or using Reuss sampling,

$$\mathbf{E}^R = \left\langle \mathbf{E}^{-1} \right\rangle^{-1} . \tag{29}$$

[6] Assuming a normal distribution.

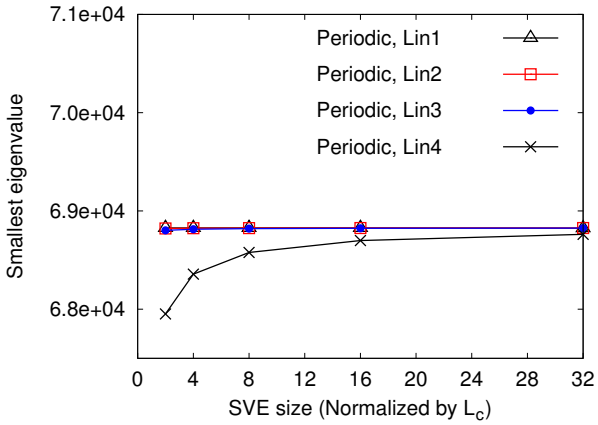


Figure 13: Convergence of effective stiffness for the periodic microstructure considered in Example 7.2.

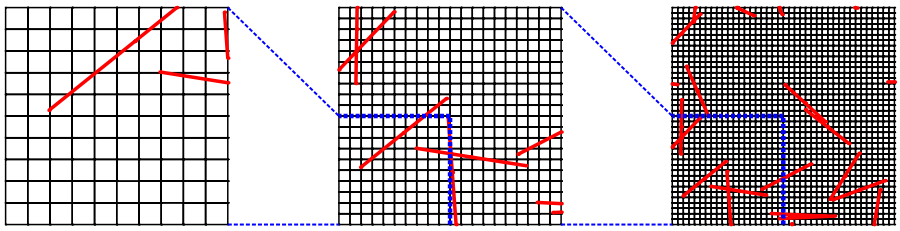

Figure 14: Statistical Volume Elements (SVEs) of different sizes for the random microstructure considered in Example 7.3.

In the above equations, $\langle \bullet \rangle \overset{\text{def}}{=} \frac{1}{N} \sum_{i=1}^{N} \bullet_i$ denotes the ensemble average of $N$ realizations.

The mean effective stiffness predicted with different BCs and discretizations is shown in Figure 17 (Voigt sampling) and Figure 18 (Reuss sampling). As one can expect, the curves are smoother than for the single realization shown in Figure 16. Weakly periodic BCs with mesh Lin5 give an improvement compared to Dirichlet BCs, but weakly periodic BCs with meshes Lin6 and Const1 give a considerable improvement compared to weakly periodic BCs with mesh Lin5. Using weakly periodic BCs in combination with Reuss sampling further improves the stiffness prediction, in particular for Const1.

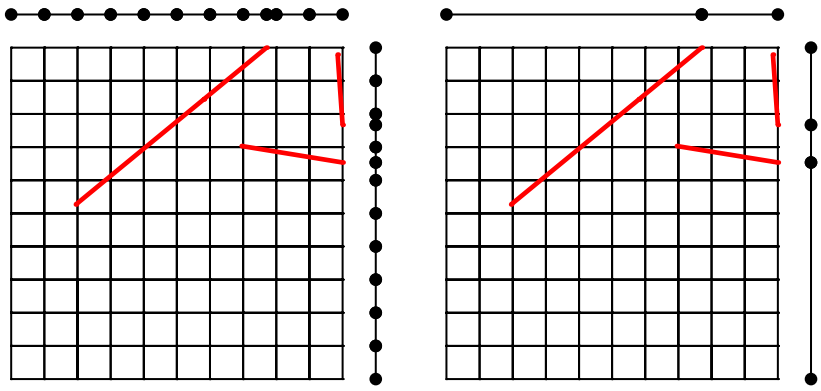

(a) Lin5 (b) Lin6 and Const1

Figure 15: Different traction discretizations considered in Example 7.3.

## 8. Summary and conclusions

In this paper, we study (first order) computational homogenization of microstructures with cracks, whereby the effective macroscale stress is obtained by solving a boundary value problem on Statistical Volume Elements (SVEs). In particular, we discuss the performance of different boundary conditions (BCs) on the SVE when cracks intersect the SVE boundary. We remark that conventional BCs (Dirichlet, Neumann, strong periodic) perform poorly when cracks intersect the SVE boundary. Therefore, we employ a weak format of microperiodicity that allows more freedom in adapting the BCs to the problem at hand.

The resulting SVE problem leads to a mixed variational format with displacements and boundary tractions as unknowns, whereby different choices for the traction approximation are possible. We choose to create a traction mesh on the image part of the SVE boundary and propose traction approximations that are piecewise constant between points where cracks intersect the boundary. The novel feature of this paper is the proposition of suitable traction approximations when cracks intersect the boundary, including the analysis of stability and accuracy properties for these approximations. In particular, we prove analytically that the LBB (inf-sup) condition is fulfilled for the chosen discretization and give a numerical example of stable and unstable approximations. We emphasize that even though the stability analysis

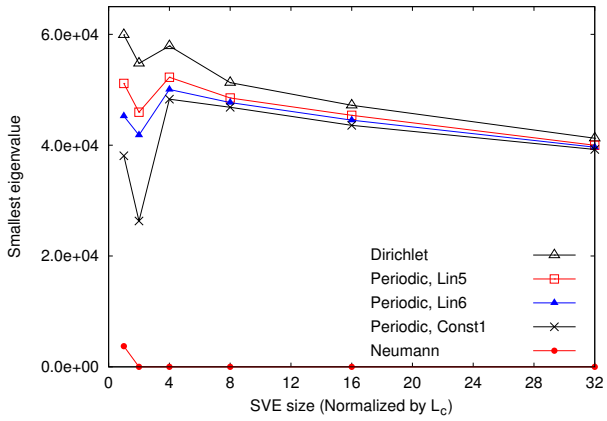


Figure 16: Effective stiffness of a random microstructure predicted with different BCs and discretizations.

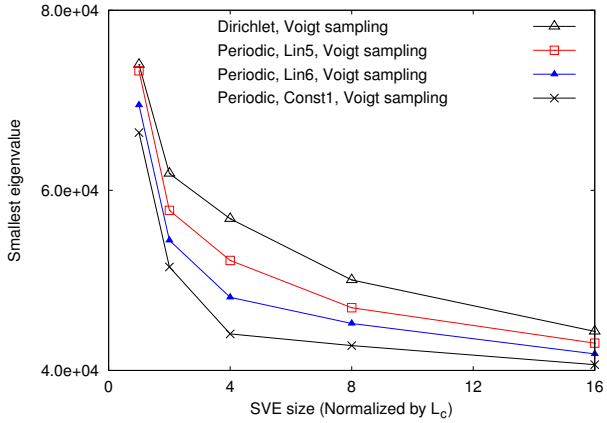


Figure 17: Effective stiffness for several realizations of a random microstructure. Mean value computed with Voigt sampling.

is carried out within the setting of weakly periodic boundary conditions, it also applies to other mixed problems with similar structure, e.g. contact problems.

With the numerical examples, we also show that the prediction of the effective stiffness depends strongly on the choice of boundary conditions and traction approximation. In particular, we demonstrate that the proposed novel traction approximation can give a substantial improvement compared to Dirichlet and strong periodic BCs, allowing for use of SVEs much smaller

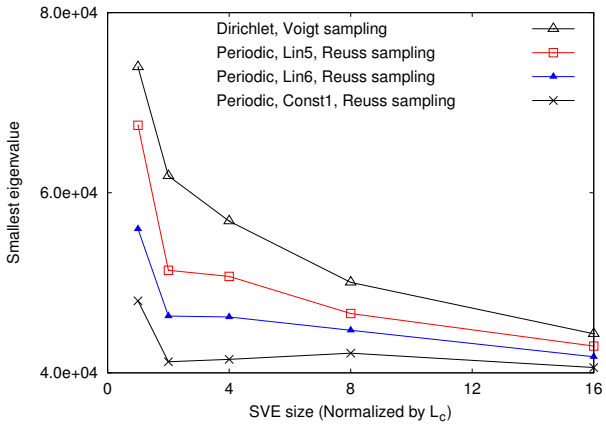


Figure 18: Effective stiffness for several realizations of a random microstructure. Mean value computed with Reuss sampling.

than what would be expected to be representative.

As for Neumann boundary conditions, we show that, (as expected), zero stiffness is predicted if cracks are located in such a way that a piece of the microstructure is completely "cut loose". As mentioned above, we propose a piecewise constant traction approximation, with traction discontinuities at corners and crack-boundary intersections. The proposed discretization is identical to Neumann BCs when no cracks intersect the boundary. In the case that cracks do intersect the boundary, the proposed piecewise constant discretization differs from Neumann BCs in the crucial sense that it does not predict zero stiffness if only a small part of the material is "cut loose" by cracks.

As to future developments, we remark that the boundary conditions proposed in this work do not enforce artificial closure of cracks on the SVE boundary. An interesting extension of the present work is to investigate how this feature affects the numerical results when crack propagation and damage progression occurs in the microstructure.

## 9. Acknowledgements

The project is financially supported by the Swedish Research Council (www.vr.se) under contract 2012-3006.

## Appendix A. Solvability

In order to complete the stability proof in Section 6.4, we will here derive the estimates for $d_{\square}(\boldsymbol{t}_\lambda, \tilde{\boldsymbol{u}})$ and $\|\tilde{\boldsymbol{u}}\|_{\mathbb{U}}$. To this end, recall the definition of $\tilde{\boldsymbol{u}}$ shown in Figure 7, where $\tilde{\boldsymbol{u}}$ is defined to be bilinear on each traction element. Furthermore, we define $\tilde{\boldsymbol{u}}$ to be zero on $\Gamma_{\square}^{-}$ as well as along the dashed blue lines in Figure 7. Next, we divide the SVE into triangles $\gamma_i$ as shown in Figure A.19, so that each traction element (index $i$) is associated to a triangle $\gamma_i$. Each triangle $\gamma_i$ is in turn split into two triangles $\gamma_i^A$ and $\gamma_i^B$.

As also shown in Figure A.19, we denote the length of the boundary segment associated to $\gamma_i^A$ and $\gamma_i^B$ by $s_i^A$ and $s_i^B$, respectively. Furthermore, we let $s_{min}$ denote the smallest value of all $s_i^A$ and $s_i^B$.

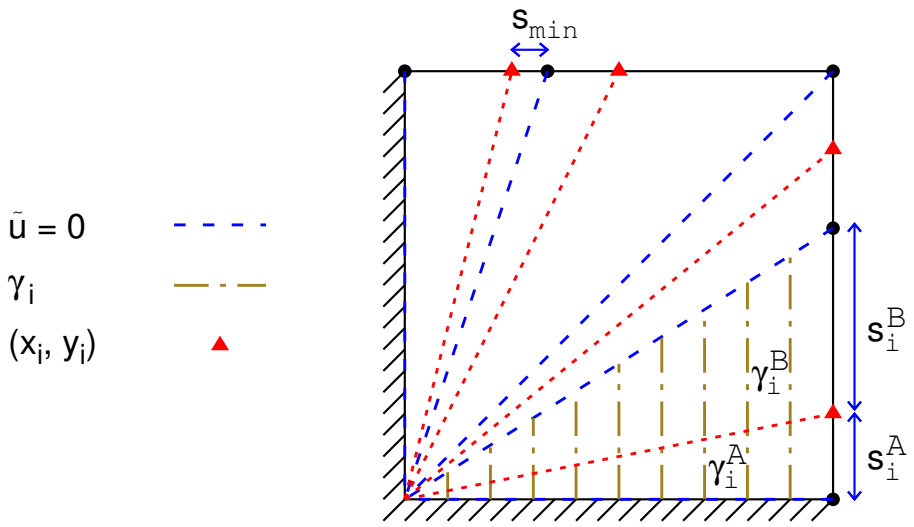


Figure A.19: Partitioning of SVE for solvability considerations: Each traction element (index $i$) is associated to a triangular part of the domain denoted by $\gamma_i$. Each triangle $\gamma_i$ is in turn split along the dashed red line intersecting $\Gamma_{\square}^{+}$ at $(x_i, y_i)$, forming two triangles $\gamma_i^A$ and $\gamma_i^B$. We also show the shortest distance $s_{min}$ between $(x_i, y_i)$ and traction discontinuities.

*Appendix A.1. Evaluation of $d_\square(\boldsymbol{t}_\lambda, \tilde{\boldsymbol{u}})$*

In order to evaluate $d_\square(\boldsymbol{t}_\lambda, \tilde{\boldsymbol{u}})$, we start from Equation (16) and note that $[\![\tilde{\boldsymbol{u}}]\!]_\square = \tilde{\boldsymbol{u}}^+ - \tilde{\boldsymbol{u}}^- = \tilde{\boldsymbol{u}}^+ - \boldsymbol{0}$. By exploiting the fact that $\boldsymbol{t}_\lambda$ is piecewise constant and noting that $\Gamma_i = \Gamma_i^A \cup \Gamma_i^B$, we get

$$\begin{aligned} d_\square(\boldsymbol{t}_\lambda, \tilde{\boldsymbol{u}}) &= \int_{\Gamma_\square^+} \boldsymbol{t}_\lambda \cdot [\![\tilde{\boldsymbol{u}}]\!]_\square \,\mathrm{d}\Gamma = \int_{\Gamma_\square^+} \boldsymbol{t}_\lambda \cdot \tilde{\boldsymbol{u}} \,\mathrm{d}\Gamma = \\ &= \sum_i \int_{\Gamma_i} \boldsymbol{t}_{\lambda i} \cdot \tilde{\boldsymbol{u}} \,\mathrm{d}\Gamma = \sum_i \boldsymbol{t}_{\lambda i} \cdot \int_{\Gamma_i} \tilde{\boldsymbol{u}} \,\mathrm{d}\Gamma = \\ &= \sum_i \boldsymbol{t}_{\lambda i} \cdot \left[ \int_{\Gamma_i^A} \tilde{\boldsymbol{u}} \,\mathrm{d}\Gamma + \int_{\Gamma_i^B} \tilde{\boldsymbol{u}} \,\mathrm{d}\Gamma \right], \end{aligned} \tag{A.1}$$

where $\boldsymbol{t}_{\lambda i}$ denotes the traction on traction element $i$. On each $\Gamma_i^A$ and $\Gamma_i^B$, $\tilde{\boldsymbol{u}}$ varies linearly between $\boldsymbol{0}$ and some maximum value $\tilde{\boldsymbol{u}}_i$. If we let $s_i \overset{\text{def}}{=} s_i^A + s_i^B$, we can therefore express Equation (A.1) as

$$\begin{aligned} \sum_i \boldsymbol{t}_{\lambda i} \cdot \left[ \int_{\Gamma_i^A} \tilde{\boldsymbol{u}} \,\mathrm{d}\Gamma + \int_{\Gamma_i^B} \tilde{\boldsymbol{u}} \,\mathrm{d}\Gamma \right] &= \sum_i \boldsymbol{t}_{\lambda i} \cdot \left[ \tilde{\boldsymbol{u}}_i \frac{s_i^A}{2} + \tilde{\boldsymbol{u}}_i \frac{s_i^B}{2} \right] = \\ &= \sum_i \frac{s_i^A + s_i^B}{2} \, \boldsymbol{t}_{\lambda i} \cdot \tilde{\boldsymbol{u}}_i = \sum_i \frac{s_i}{2} \, \boldsymbol{t}_{\lambda i} \cdot \tilde{\boldsymbol{u}}_i. \end{aligned} \tag{A.2}$$

Recall that the purpose is to choose a clever $\tilde{\boldsymbol{u}}$ in order to prove Equation (19) via Equation (22). The choice $\tilde{\boldsymbol{u}}_i = 2\boldsymbol{t}_{\lambda i}$ inserted in Equation (A.2) results in

$$d_\square(\boldsymbol{t}_\lambda, \tilde{\boldsymbol{u}}) = \sum_i \frac{s_i}{2} \, \boldsymbol{t}_{\lambda i} \cdot \tilde{\boldsymbol{u}}_i = \sum_i (\boldsymbol{t}_{\lambda i} \cdot \boldsymbol{t}_{\lambda i}) \, s_i = \int_{\Gamma_\square^+} \boldsymbol{t}_\lambda \cdot \boldsymbol{t}_\lambda \,\mathrm{d}\Gamma = \|\boldsymbol{t}_\lambda\|_{\mathbb{T}}^2. \tag{A.3}$$

*Appendix A.2. Estimation of bound for $\|\tilde{\boldsymbol{u}}\|_{\mathbb{U}}$*

In order to compute a bound for $\|\tilde{\boldsymbol{u}}\|_{\mathbb{U}}$, we start from

$$\|\tilde{\boldsymbol{u}}\|_{\mathbb{U}} = \sqrt{a_\square(\tilde{\boldsymbol{u}}, \tilde{\boldsymbol{u}})} = \sqrt{\int_\Omega \boldsymbol{\epsilon} : \mathbf{E} : \boldsymbol{\epsilon} \,\mathrm{d}\Omega}. \tag{A.4}$$

By splitting the domain into triangles as described previously, we may evaluate Equation (A.4) as

$$\|\tilde{\boldsymbol{u}}\|_{\mathbb{U}} = \sqrt{\sum_i \left( \int_{\gamma_i^A} \boldsymbol{\epsilon} : \mathbf{E} : \boldsymbol{\epsilon} \,\mathrm{d}\Omega + \int_{\gamma_i^B} \boldsymbol{\epsilon} : \mathbf{E} : \boldsymbol{\epsilon} \,\mathrm{d}\Omega \right)}. \tag{A.5}$$

Below, we utilize that the strain is piecewise constant on each triangle, and can be expressed in terms of the traction amplitude $\boldsymbol{t}_i$.

*Appendix A.2.1. Evaluation of the strain on $\gamma_i^A$*

Consider a triangle $\gamma_i^A$ with an associated part of the boundary $\Gamma_i^A$. Let the boundary part be located at $x = L_\square$. The displacement varies linearly according to

$$\tilde{u}_\alpha = A_{1\alpha} + A_{2\alpha} x + A_{3\alpha} y, \tag{A.6}$$

where $\alpha$ denotes $x-$ or $y-$direction. The conditions on the displacement at the triangle corners allow us to solve for the coefficients as follows:

$$\begin{cases} \tilde{u}_\alpha(0,0) = 0 \\ \tilde{u}_\alpha\big(L_\square, y_i - s_i^A\big) = 0 \\ \tilde{u}_\alpha(L_\square, y_i) = \tilde{u}_{\alpha i} \end{cases} \Rightarrow \begin{cases} A_{1\alpha} = 0 \\ A_{2\alpha} = (\tilde{u}_{\alpha i}/L_\square)(1 - y_i/s_i^A) \\ A_{3\alpha} = \tilde{u}_{\alpha i}/s_i^A \end{cases}$$

Hence, the displacement in a triangle $\gamma_i^A$ is given by

$$\tilde{u}_\alpha = (\tilde{u}_{\alpha i}/L_\square)(1 - y_i/s_i^A)x + \frac{\tilde{u}_{\alpha i}}{s_i^A} y.$$

The components of the displacement gradient are trivially obtained as

$$\frac{\partial\, \tilde{u}_\alpha}{\partial x} = (\tilde{u}_{\alpha i}/L_\square)(1 - y_i/s_i^A), \qquad \frac{\partial\, \tilde{u}_\alpha}{\partial y} = \frac{\tilde{u}_{\alpha i}}{s_i^A}.$$

The (Euclidean) norm of the strain[7] in a triangle $\gamma_i^A$ is bounded by

$$|\boldsymbol{\epsilon}_i^A| = |[\boldsymbol{u} \otimes \boldsymbol{\nabla}]^{sym}| = \sqrt{\left(\frac{\tilde{u}_{xi}}{L_\square}\left(1-\frac{y_i}{s_i^A}\right)\right)^2 + \frac{1}{2}\left(\frac{\tilde{u}_{yi}}{L_\square}\left(1-\frac{y_i}{s_i^A}\right)+\frac{\tilde{u}_{xi}}{s_i^A}\right)^2 + \left(\frac{\tilde{u}_{yi}}{s_i^A}\right)^2} =$$

$$= \frac{1}{s_i^A}\sqrt{\frac{\tilde{u}_{xi}^2}{L_\square^2}\left(s_i^A - y_i\right)^2 + \frac{1}{2}\frac{\tilde{u}_{yi}^2}{L_\square^2}\left(s_i^A - y_i\right)^2 + \frac{\tilde{u}_{yi}}{L_\square}\left(s_i^A - y_i\right)\tilde{u}_{xi} + \frac{1}{2}\tilde{u}_{xi}^2 + \tilde{u}_{yi}^2}$$

$$\leq \frac{1}{s_i^A}\sqrt{\frac{\tilde{u}_{xi}^2}{L_\square^2}\left|s_i^A - y_i\right|^2 + \frac{1}{2}\frac{\tilde{u}_{yi}^2}{L_\square^2}\left|s_i^A - y_i\right|^2 + \frac{|\tilde{u}_{yi}|}{L_\square}\left|s_i^A - y_i\right||\tilde{u}_{xi}| + \frac{1}{2}\tilde{u}_{xi}^2 + \tilde{u}_{yi}^2}$$

$$\left\{\text{Insert that } |\tilde{u}_{xi}| \leq |\tilde{\boldsymbol{u}}_i|, |\tilde{u}_{yi}| \leq |\tilde{\boldsymbol{u}}_i| \text{ and } \left|s_i^A - y_i\right| \leq L_\square\right\}$$

$$\leq \frac{1}{s_i^A}\sqrt{\frac{|\tilde{\boldsymbol{u}}_i|^2}{L_\square^2}L_\square^2 + \frac{1}{2}\frac{|\tilde{\boldsymbol{u}}_i|^2}{L_\square^2}L_\square^2 + \frac{|\tilde{\boldsymbol{u}}_i|}{L_\square}L_\square|\tilde{\boldsymbol{u}}_i| + \frac{1}{2}|\tilde{\boldsymbol{u}}_i|^2 + |\tilde{\boldsymbol{u}}_i|^2}$$

$$\leq \frac{|\tilde{\boldsymbol{u}}_i|}{s_i^A}\sqrt{1+\frac{1}{2}+1+\frac{1}{2}+1} = 2\frac{|\tilde{\boldsymbol{u}}_i|}{s_i^A}.$$

Inserting the choice $\tilde{\boldsymbol{u}}_i = 2\boldsymbol{t}_{\lambda i}$, we obtain

$$|\boldsymbol{\epsilon}_i^A| \leq 2\frac{|2\boldsymbol{t}_{\lambda i}|}{s_i^A} = 4\frac{|\boldsymbol{t}_{\lambda i}|}{s_i^A}. \tag{A.7}$$

Clearly, the same procedure can be carried out for a triangle sharing an edge with the part of $\Gamma_\square^+$ parallel to the x-axis.

*Appendix A.2.2. Evaluation of the strain on $\gamma_i^B$*

Consider a triangle $\gamma_i^B$ with an associated part of the boundary $\Gamma_i^B$. Let the boundary part be located at $x = L_\square$. The displacement varies linearly according to

$$\tilde{u}_\alpha = A_{4\alpha} + A_{5\alpha}x + A_{6\alpha}y,$$

where $\alpha$ denotes $x-$ or $y-$direction. We may employ the same procedure as in Appendix A.2.1 to solve for the coefficients:

$$\begin{cases} \tilde{u}_\alpha(0,0) = 0 \\ \tilde{u}_\alpha(L_\square, y_i) = \tilde{u}_{\alpha i} \\ \tilde{u}_\alpha\left(L_\square, y_i + s_i^B\right) = 0 \end{cases} \Rightarrow \begin{cases} A_{4\alpha} = 0 \\ A_{5\alpha} = (\tilde{u}_{\alpha i}/L_\square)(1 + y_i/s_i^B) \\ A_{6\alpha} = -\tilde{u}_{\alpha i}/s_i^B \end{cases}$$

[7] We simply define the norm of the strain tensor as $|\boldsymbol{\epsilon}| = \sqrt{\boldsymbol{\epsilon} : \boldsymbol{\epsilon}}$.

Therefore, the displacement in a triangle $\gamma_i^B$ is given by

$$\tilde{u}_\alpha = \frac{\tilde{u}_{\alpha i}}{L_\square}\left(1 + \frac{y_i}{s_i^B}\right)x - \frac{\tilde{u}_{\alpha i}}{s_i^B}y,$$

so that the displacement gradient can be computed as

$$\frac{\partial\,\tilde{u}_\alpha}{\partial x} = \frac{\tilde{u}_{\alpha i}}{L_\square}\left(1 + \frac{y_i}{s_i^B}\right), \qquad \frac{\partial\,\tilde{u}_\alpha}{\partial y} = -\frac{\tilde{u}_{\alpha i}}{s_i^B}.$$

Following the same procedure as in Appendix A.2.1 and noting that $s_i^B + y_i \leq L_\square$, we compute a bound for the strain as

$$\begin{aligned}
|\boldsymbol{\epsilon}| &= \sqrt{\left(\frac{\tilde{u}_{xi}}{L_\square}\left(1 + \frac{y_i}{s_i^B}\right)\right)^2 + \frac{1}{2}\left(\frac{\tilde{u}_{yi}}{L_\square}\left(1 + \frac{y_i}{s_i^B}\right) - \frac{\tilde{u}_{xi}}{s_i^B}\right)^2 + \left(\frac{\tilde{u}_{yi}}{s_i^B}\right)^2} \\
&\leq \frac{|\tilde{\boldsymbol{u}}_i|}{s_i^B}\sqrt{\frac{3}{2}\left(\frac{1}{L_\square}\left(s_i^B + y_i\right)\right)^2 + \frac{1}{L_\square}\left(s_i^B + y_i\right) + \frac{3}{2}} \\
&\leq \frac{|\tilde{\boldsymbol{u}}_i|}{s_i^B}\sqrt{\frac{3}{2}\left(\frac{1}{L_\square}\left(L_\square\right)\right)^2 + \frac{1}{L_\square}\left(L_\square\right) + \frac{3}{2}} \\
&= 2\frac{|\tilde{\boldsymbol{u}}_i|}{s_i^B}.
\end{aligned}$$

In summary, we have the estimate

$$|\boldsymbol{\epsilon}_i^B| \leq 2\frac{|\tilde{\boldsymbol{u}}_i|}{s_i^B} = 4\frac{|\boldsymbol{t}_{\lambda i}|}{s_i^B}.$$

*Appendix A.2.3. Evaluation of bound for* $\|\boldsymbol{u}\|_{\mathbb{U}}$

For a piece $\gamma_i^A$, we have

$$\begin{aligned}
\int_{\gamma_i^A} \boldsymbol{\epsilon} : \mathbf{E} : \boldsymbol{\epsilon}\,\mathrm{d}\Omega &\leq \lambda_{max}|\boldsymbol{\epsilon}|^2 A = \lambda_{max}|\boldsymbol{\epsilon}|^2\frac{L_\square s_i^A}{2} \\
&\leq \lambda_{max}\left(4\frac{|\boldsymbol{t}_{\lambda i}|}{s_i^A}\right)^2\frac{L_\square s_i^A}{2} = 8\lambda_{max}\frac{|\boldsymbol{t}_{\lambda i}|^2 L_\square}{s_i^A},
\end{aligned}$$

where $|\boldsymbol{\epsilon}|$ is constant over the triangle and bounded according to Appendix A.2.1, and $\lambda_{max}$ is the largest eigenvalue of the stiffness tensor anywhere in

the domain $\Omega_\square$. Similarly, from Appendix A.2.2, we conclude for a piece $\gamma_i^B$ that

$$\int_{\gamma_i^B} \boldsymbol{\epsilon} : \mathbf{E} : \boldsymbol{\epsilon} \, \mathrm{d}\Omega \leq 8\lambda_{max} \frac{|\boldsymbol{t}_{\lambda i}|^2 L_\square}{s_i^B}.$$

Now return to the expression for $\|\boldsymbol{u}\|_{\mathbb{U}}$ in Equation (A.5):

$$\begin{aligned}
\|\boldsymbol{u}\|_{\mathbb{U}} &= \sqrt{\sum_i \int_{\gamma_i^A} \boldsymbol{\epsilon} : \mathbf{E} : \boldsymbol{\epsilon} \, \mathrm{d}\Omega + \int_{\gamma_i^B} \boldsymbol{\epsilon} : \mathbf{E} : \boldsymbol{\epsilon} \, \mathrm{d}\Omega} \\
&\leq \sqrt{\sum_i 8\lambda_{max} \frac{|\boldsymbol{t}_{\lambda i}|^2 L_\square}{s_i^A} + 8\lambda_{max} \frac{|\boldsymbol{t}_{\lambda i}|^2 L_\square}{s_i^B}} \\
&\leq \sqrt{8\lambda_{max} \frac{L_\square}{s_{min}^2} \sum_i \left(s_i^A + s_i^B\right) |\boldsymbol{t}_{\lambda i}|^2} \\
&= \underbrace{\sqrt{8\lambda_{max} \frac{L_\square}{s_{min}^2}}}_{\stackrel{\text{def}}{=} C_1} \|\boldsymbol{t}_\lambda\|_{\mathbb{T}}.
\end{aligned}$$

In short, we have

$$\|\boldsymbol{u}\|_{\mathbb{U}} \leq C_1 \|\boldsymbol{t}_\lambda\|_{\mathbb{T}},$$

where

$$C_1 = \sqrt{\frac{8\lambda_{max} L_\square}{s_{min}^2}}.$$

Since $C_1 > 0$ and independent of the mesh size, we now have the results we need to complete the stability proof in Section 6.4.


[1] M. Geers, V. Kouznetsova, W. Brekelmans, Multi-scale computational homogenization: Trends and challenges, Journal of Computational and Applied Mathematics 234 (7) (2010) 2175–2182.

[2] T. Zohdi, P. Wriggers, A model for simulating the deterioration of structural-scale material responses of microheterogeneous solids, Computer Methods in Applied Mechanics and Engineering 190 (22-23) (2001) 2803–2823.

[3] M. Ostoja-Starzewski, Material spatial randomness: From statistical to representative volume element, Probabilistic Engineering Mechanics 21 (2) (2006) 112–132.

[4] J. Fish, K. Shek, M. Pandheeradi, M. S. Shephard, Computational plasticity for composite structures based on mathematical homogenization: Theory and practice, Computer Methods in Applied Mechanics and Engineering 148 (1-2) (1997) 53–73.

[5] C. Miehe, A. Koch, Computational micro-to-macro transitions of discretized microstructures undergoing small strains, Archive of Applied Mechanics (Ingenieur Archiv) 72 (4-5) (2002) 300–317.

[6] I. Babuška, B. Andersson, P. J. Smith, K. Levin, Damage analysis of fiber composites part I: Statistical analysis on fiber scale, Computer Methods in Applied Mechanics and Engineering 172 (1-4) (1999) 27–77.

[7] . Temizer, T. Wu, P. Wriggers, On the optimality of the window method in computational homogenization, International Journal of Engineering Science 64 (2013) 66–73.

[8] J. C. Simo, J. Oliver, F. Armero, An analysis of strong discontinuities induced by strain-softening in rate-independent inelastic solids, Computational Mechanics 12 (5) (1993) 277–296.

[9] M. Ortiz, A. Pandolfi, Finite-deformation irreversible cohesive elements for three-dimensional crack-propagation analysis, International Journal for Numerical Methods in Engineering 44 (9) (1999) 1267–1282.

[10] T. Belytschko, T. Black, Elastic crack growth in finite elements with minimal remeshing, International Journal for Numerical Methods in Engineering 45 (5) (1999) 601–620.

[11] I. Babuska, G. Caloz, J. E. Osborn, Special finite element methods for a class of second order elliptic problems with rough coefficients, SIAM Journal on Numerical Analysis 31 (4) (1994) 945–981.

[12] T. Fries, T. Belytschko, The extended/generalized finite element method: an overview of the method and its applications, International Journal for Numerical Methods in Engineering 84 (3) (2010) 253–304.

[13] N. Moës, J. Dolbow, T. Belytschko, A finite element method for crack growth without remeshing, International Journal for Numerical Methods in Engineering 46 (1) (1999) 131–150.

[14] C. Daux, N. Moës, J. Dolbow, N. Sukumar, T. Belytschko, Arbitrary branched and intersecting cracks with the extended finite element method, International Journal for Numerical Methods in Engineering 48 (12) (2000) 1741–1760.

[15] J. Dolbow, N. Moës, T. Belytschko, An extended finite element method for modeling crack growth with frictional contact, Computer Methods in Applied Mechanics and Engineering 190 (51-52) (2001) 6825–6846.

[16] E. Coenen, V. Kouznetsova, M. Geers, Novel boundary conditions for strain localization analyses in microstructural volume elements, International Journal for Numerical Methods in Engineering 90 (1) (2012) 1–21.

[17] E. W. C. Coenen, V. G. Kouznetsova, E. Bosco, M. G. D. Geers, A multiscale approach to bridge microscale damage and macroscale failure: a nested computational homogenization-localization framework, International Journal of Fracture 178 (1-2) (2012) 157–178.

[18] E. Bosco, V. G. Kouznetsova, E. W. C. Coenen, M. G. D. Geers, A. Salvadori, A multiscale framework for localizing microstructures towards the onset of macroscopic discontinuity, Computational Mechanics 54 (2) (2014) 299–319.

[19] T. Belytschko, S. Loehnert, J.-H. Song, Multiscale aggregating discontinuities: A method for circumventing loss of material stability, International Journal for Numerical Methods in Engineering 73 (6) (2008) 869–894.

[20] F. Larsson, K. Runesson, F. Su, Variationally consistent computational homogenization of transient heat flow, International Journal for Numerical Methods in Engineering 81 (13) (2010) 1659–1686.

[21] F. Larsson, K. Runesson, S. Saroukhani, R. Vafadari, Computational homogenization based on a weak format of micro-periodicity for RVE-problems, Computer Methods in Applied Mechanics and Engineering 200 (1-4) (2011) 11–26.

[22] C. Sandstom, F. Larsson, K. Runesson, Weakly periodic boundary conditions for the homogenization of flow in porous media, Advanced Modeling and Simulation in Engineering Sciences 1 (1) (2014) 12.

[23] M. Öhman, K. Runesson, F. Larsson, On the variationally consistent computational homogenization of elasticity in the incompressible limit, Advanced Modeling and Simulation in Engineering Sciences 2 (1) (2015) 1–29.

[24] P. M. A. Areias, T. Belytschko, Analysis of three-dimensional crack initiation and propagation using the extended finite element method, International Journal for Numerical Methods in Engineering 63 (2005) 760–788.

[25] N. El-Abbasi, K.-J. Bathe, Stability and patch test performance of contact discretizations and a new solution algorithm, Computers & Structures 79 (16) (2001) 1473–1486.

[26] B. Patzák, Z. Bittnar, Design of object oriented finite element code, Advances in Engineering Software 32 (10-11) (2001) 759–767.

[27] B. Patzák, OOFEM project home page: www.oofem.org (2000).
URL `http://www.oofem.org`